Computational Study of Some Urolithin Derivatives-based Biomass Corrosion Inhibitors on the Fe (110), Cu(111) and Al(111) Surface

Rebaz A. Omer†

Department of Chemistry, Faculty of Science and Health, Koya University,
Koya, Kurdistan Region – F.R. Iraq

***Abstract*—Corrosion poses a significant economic and environmental burden, highlighting the need for sustainable corrosion inhibitors. This study investigates the potential of urolithin derivatives (UroE, UroM5, UroM6, and UroM7) as eco-friendly corrosion inhibitors for Fe(110), Cu(111), and Al(111) surfaces. The research uses density functional theory calculations and Monte Carlo (MC) simulations to compute quantum chemical parameters, Fukui function, and non-covalent interactions. The results show that compounds with strong hydrogen bonding interactions form more robust bonds with the metal surface, potentially leading to enhanced corrosion protection. UroM5 demonstrates superior stability and lower reactivity due to its high band gap energy. MC simulations reveal that the adsorption energies of urolithin derivatives on metal surfaces follow a trend: UroM5 > UroM6 > UroE > UroM7, suggesting a stronger binding affinity for these metals. Thermal characteristics, particularly Gibbs free energy, are also investigated. The results suggest that a temperature increase from 825 to 1000 K may induce a transition from physisorption to chemisorption for all chemicals on the metal surface. These comprehensive analyses provide valuable insights into the mechanism and efficiency of urolithin derivatives as corrosion inhibitors, paving the way for the development of novel and eco-friendly anti-corrosion materials.**

***Index Terms*—Urolithins, Density functional theory, Fukui function, Global reactivity, Monte Carlo simulations. Anti-Corrosion**

I. Introduction

The phenomenon of corrosion, which refers to the degradation of metals caused by their contact to corrosive substances such as acids, presents substantial economic and environmental challenges. The scope of this matter encompasses not just metals, but also non-metallic substances such as plastics, ceramics, concrete, and rubber (Predko, et al., 2021; Kareem, et al., 2024). Corrosion inhibitors may safeguard metals or alloys by altering their quantum chemical characteristics. Some corrosion inhibitors, for example, may adsorb onto the metal's surface and establish a protective barrier, preventing corrosive species from reaching the metal's surface. Researchers may discover new and more effective corrosion protection methods (Özbakır Işın, et al., 2020; İsen, et al., 2023, Koparir, et al., 2023). Historically, corrosion inhibitors have often used organic compounds that include heteroatoms (namely oxygen, nitrogen, phosphorus, and sulfur) and π-bonds. This is attributed to their capacity to create a protective coating on metal surfaces (El Aoufir, et al., 2017). The presence of this layer impedes the movement of oxygen and water, thereby impeding the corrosion mechanism caused by the disparity in potential energies between the metal and its corrosive derivatives. Corrosion inhibitors are sometimes included into paints to enhance their protective properties (Murthy and Vijayaragavan, 2014).

Corrosion inhibition has been extensively studied using both experimental and theoretical approaches. Weight-loss and electrochemical techniques are common experimental methods. Carbon steel, mild steel, copper, zinc, and aluminum are frequently investigated metals (Chen, et al., 2019, Hazani, et al., 2019, Guruprasad, et al., 2020, Tasić, et al., 2019, Uwiringiyimana, Joseph and ADams, 2016).

In recent years, research has focused on exploring "green corrosion inhibitors" as a sustainable alternative to potentially toxic organic substances. This approach leverages the inherent eco-friendliness of certain drugs, which often possess heterocyclic groups that effectively inhibit corrosion (Hameed, Abu-Nawwas and Shehata, 2013; Rani and Basu, 2012). In addition, the widespread availability and affordability of drugs make them attractive candidates for this application. Moreover, studies have shown that the effectiveness of organic corrosion inhibitors increases with higher concentrations (Uwiringiyimana, Joseph and ADams, 2016).

Rani and Basu (2012) attributed the efficacy of organic corrosion inhibitors to their high basicity, electron density, specific chemical structures, and physicochemical properties. To understand how these molecules inhibit corrosion, researchers have developed theoretical models

ARO-The Scientific Journal of Koya University
Vol. XIII, No. 1 (2025), Article ID: ARO.11828. 17 pages
DOI: 10.14500/aro.11828
Received: 19 September 2024; Accepted: 12 January 2025
Regular research paper; Published: 06 February 2025
†Corresponding author's e-mail: rebaz.anwar@koyauniversity.org

based on quantum mechanics. One such approach, the frontier molecular orbital theory, uses quantum mechanical calculations to investigate the corrosion inhibition potential of various drugs on metal surfaces, such as Fe(110), Cu(111), and Al(111) (Uwiringiyimana, Joseph and ADams, 2016; Rasul, et al., 2023).

Urolithins are bioactive phenolic compounds that originate as microbial metabolites from the consumption of pomegranate and certain berries. They belong to the 6H-dibenzo[b,d]pyran-6-one family and have gained significant scientific interest due to their diverse biological properties and potential health benefits. Among the natural urolithins identified, structural modifications primarily involve the hydroxyl and lactone groups, enabling researchers to explore their functional diversity. These modifications have led to the discovery of urolithin derivatives with enhanced biological activities, making them promising candidates for further investigation in therapeutic, industreal and nutritional applications (Xiangrong, Zhuanhong and Lei, 2023; Norouzbahari, et al., 2018).

This study employs density functional theory (DFT) and Monte Carlo simulations to evaluate the corrosion inhibition potential of urolithin derivatives (UroE, UroM-5, UroM-6, and UroM-7) see Fig. 1 on Fe(110), Cu(111), and Al(111) surfaces. By analyzing surface energies, HOMO-LUMO characteristics, and derived parameters such as electronegativity, hardness, softness, and charge transfer, the investigation aims to elucidate the corrosion inhibition mechanisms of these compounds. This research pioneers the exploration of urolithin derivatives as eco-friendly corrosion inhibitors for these metals, providing innovative insights into sustainable corrosion management.

II. Computational Study

A. DFT

For the purpose of visualization, the molecular geometries of compounds S1–S8 were drawn out using GaussView 6.0 software to predict their potential for corrosion inhibition (Dennington, Keith and Millam, 2016). Gaussian 09, Revision D.01 was used to get optimal performance in the gas phase for these structures, (Frisch and Clemente) (Frisch et al., 2013) with the DFT/B3LYP/6-311++G(d,p) approach (Krishnan, et al., 1980, Becke, 1996, Frisch, Pople and Binkley, 1984). The HOMO, LUMO, and molecular electrostatic potential (MEP) surfaces were created using the optimized structures and GaussView 6.0 (Dennington, Keith and Millam, 2016, Omer, et al., 2024). The optimized and geometric structures of these molecules and calculated various parameters including energy gap(Ediff), global hardness (η), global softness (S), electronegativity (χ), chemical potential (μ), electrophilicity (ω), and nucleophilicity (ε), $\Delta E_{back\text{-}donation}$, reactivity, provide valuable insights into a molecule's stability, maximal amount of electronic charge (ΔN_{max}), and selectivity through the software as seen by Equations 1-10.

$$I = -E_{HOMO} \text{ and } A = -E_{LUMO} \quad (1)$$

$$\Delta E_{diff} = E_{LUMO} - E_{HOMO} \quad (2)$$

$$\chi_{inh} = \frac{E_{HOMO} + E_{LUMO}}{2} \quad (3)$$

$$\mu = -\frac{\left(E_{HOMO} + E_{LUMO}\right)}{2} \quad (4)$$

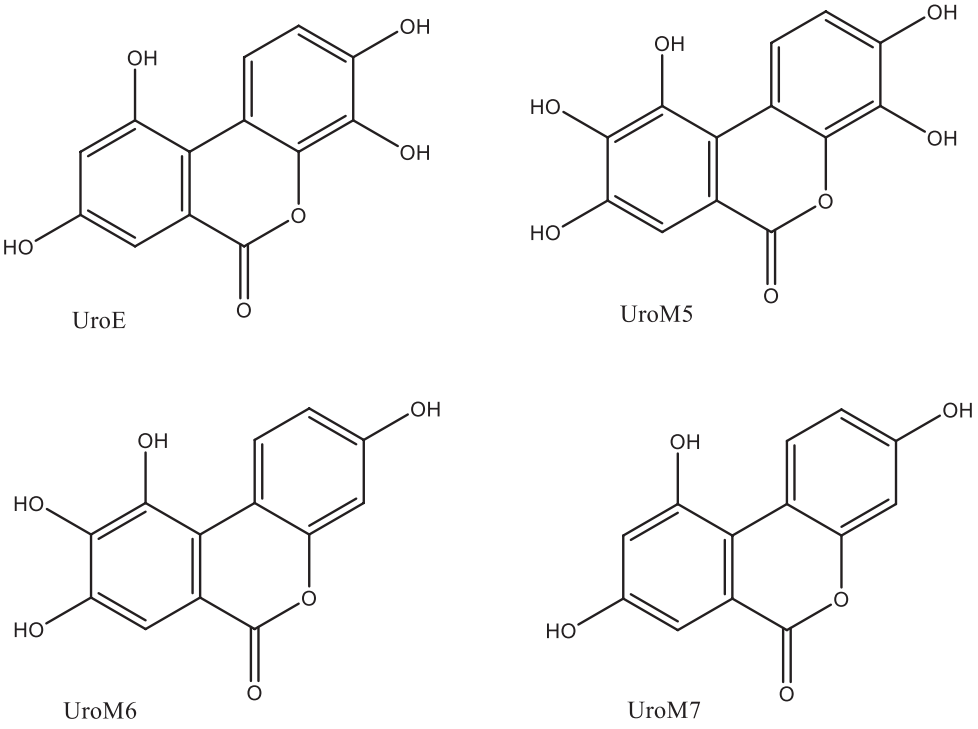

Fig. 1. The chemical structures of the urolithin derivatives analyzed in this study.

$$\eta_{Inh} = \frac{\Delta E_{gap}}{2} \tag{5}$$

$$S = \frac{1}{2\eta_{inh}} \tag{6}$$

$$\omega_{inh} = \frac{\chi_{inh}^2}{2\eta_{inh}} \tag{7}$$

$$\Delta N = \frac{\phi_{Fe} - \chi_{inh}}{2\left(\eta_{Fe} + \eta_{inh}\right)} \tag{8}$$

$$\Delta \psi = -\frac{\left(\phi_{Fe} - \chi_{inh}\right)^2}{4\left(\eta_{Fe} + \eta_{inh}\right)} \tag{9}$$

$$\Delta E_{back-donation} = \frac{-\eta}{4} \tag{10}$$

When applied in this particular context, the symbols Φ_{Fe} and η_{Fe} represent the work function and absolute hardness of the iron (Fe) metal, respectively, with values of (Φ_{Fe} = 4.82) (Ech-Chihbi, et al., 2024), and the global hardness of Fe (η_{Fe}) theoretical values are η_{Fe} = 0 eV, assuming that IA = EA for metallic bulk atoms (Boughoues, et al., 2020).

B. Topological Parameters

The Monte Carlo simulations were carried out with the Adsorption Locator module within the Material Studio software. This computational setup employs the Metropolis algorithm to model the adsorption process (Gowers, et al., 2018). Each iteration consists of simulated annealing, executed over 50,000 steps. For energy evaluations and to search for equilibrium configurations, the COMPASSIII force field was applied (Sun, et al., 2016). To precisely assess electrostatic interactions, the Ewald method was implemented, achieving an accuracy of 10–5 kcal/mol (Nam, Gao and York, 2005).

III. Results and Discussion

A. Non-covalent Interactions (NCI) and Reduced Density Gradient (RDG) Analysis

NCI and RDG are novel methods for analyzing weak intermolecular interactions. The NCI index characterizes and evaluates the properties of weak interactions, while the RDG index supports the presence of non-covalent interactions. RDG is a fundamental dimensionless parameter that encompasses both the density and its initial derivative eq. (11). (Domingo, et al., 2002; Asath, et al., 2016; Boukabcha, et al., 2023; Asif, et al., 2023):

$$RDG(r) = \frac{1|\nabla\rho(r)|}{2\left(3\pi r^2\right)^{\frac{1}{3}}\rho^{\frac{4}{3}}(r)} \tag{11}$$

The Multiwfn program was used to generate the colorful RDG scatter plots (Lu and Chen, 2012). While the VMD program was used to create a visual illustration of the 3D isosurface (Humphrey, Dalke and Schulten, 1996). The visual representations of the two-dimensional RDG plots and the three-dimensional isosurface are shown in Fig. 2. The RDG scatter can be used to study the corrosion inhibition mechanism of all urolithins. The RDG scatter can be used to identify the regions of the metal surfaces (Fe(110), Cu (111), and Al (111) where the urolithins are adsorbing and to study the effect of the urolithins on the electron density of the metal surface. Red, blue, and green colors in RDG scatter plots for Urolithins can be used to study and predict their corrosion inhibition properties. The red color in RDG scatter plots indicates regions of high electron density. These regions are more likely to be involved in chemical reactions and thus more susceptible to corrosion. Urolithins (E, M5, M6, M7) that can effectively adsorb to the red regions of a metal surface are likely to be effective corrosion inhibitors. As well as the Blue color in RDG scatter plots indicates regions of low electron density. These regions are less likely to be involved in chemical reactions and thus less susceptible to corrosion. However, blue regions can still play a role in corrosion by providing a pathway for corrosive species to reach the more reactive red regions. Moreover, the Green color in RDG scatter plots is typically used to represent intermediate electron density regions. These regions may or may not play a role in corrosion (Saidj, et al., 2023; Boukabcha, et al., 2023). The positive sign of lambda (λ) indicates that the electrons are localized, while the negative sign of λ indicates that the electrons are delocalized. In the context of corrosion, the localized electrons are more likely to react with corrosive species and thus more susceptible to corrosion. Based on the results shown in Fig. 2, it is clear that the examined compounds exhibit a significant number of green and red spots. These visual characteristics can be attributed to the high prevalence of van der Waals interactions and the observed steric effects within the molecule. However, the greater number of blue spots indicates a higher number of strong hydrogen bonds throughout the entire compound. On the other hand, NCI-RDG scatter plots show red patches that correspond to strong repulsive forces inside aromatic rings. The green isosurface represents van der Waals (vdW) interactions involving hydrogen-hydrogen (H-H), nitrogen-hydrogen (N-H) bonds, and other associated interactions, which are somewhat weaker.

B. Topological Parameters

Atoms in molecules (AIM) analysis is a widely used method for identifying and describing non-covalent interactions within molecular systems, with a particular focus on intra- and intermolecular hydrogen bonds. AIM identifies and characterizes hydrogen bonds in molecular complexes by comprehensively analyzing electron density using topological methods (Tang and Zhu, 2021; Jumabaev, et al., 2023; Bader, 2010). We used the B3LYP methodology to compute the topological properties of bond critical points (BCPs), including the Laplacian of electron density, electron density, potential energy density, and ellipticity. Table I summarizes the calculations, and Fig. 3 shows the BCPs for the neutral and protonated states. Rozas, Alkorta and Elguero, 2000 classify hydrogen bonds as weak, medium, and strong based on the electron density and Hamiltonian at the BCP. Weak hydrogen bonds have a positive electron density and a positive Hamiltonian, and an interaction energy

http://dx.doi.org/10.14500/aro.11828

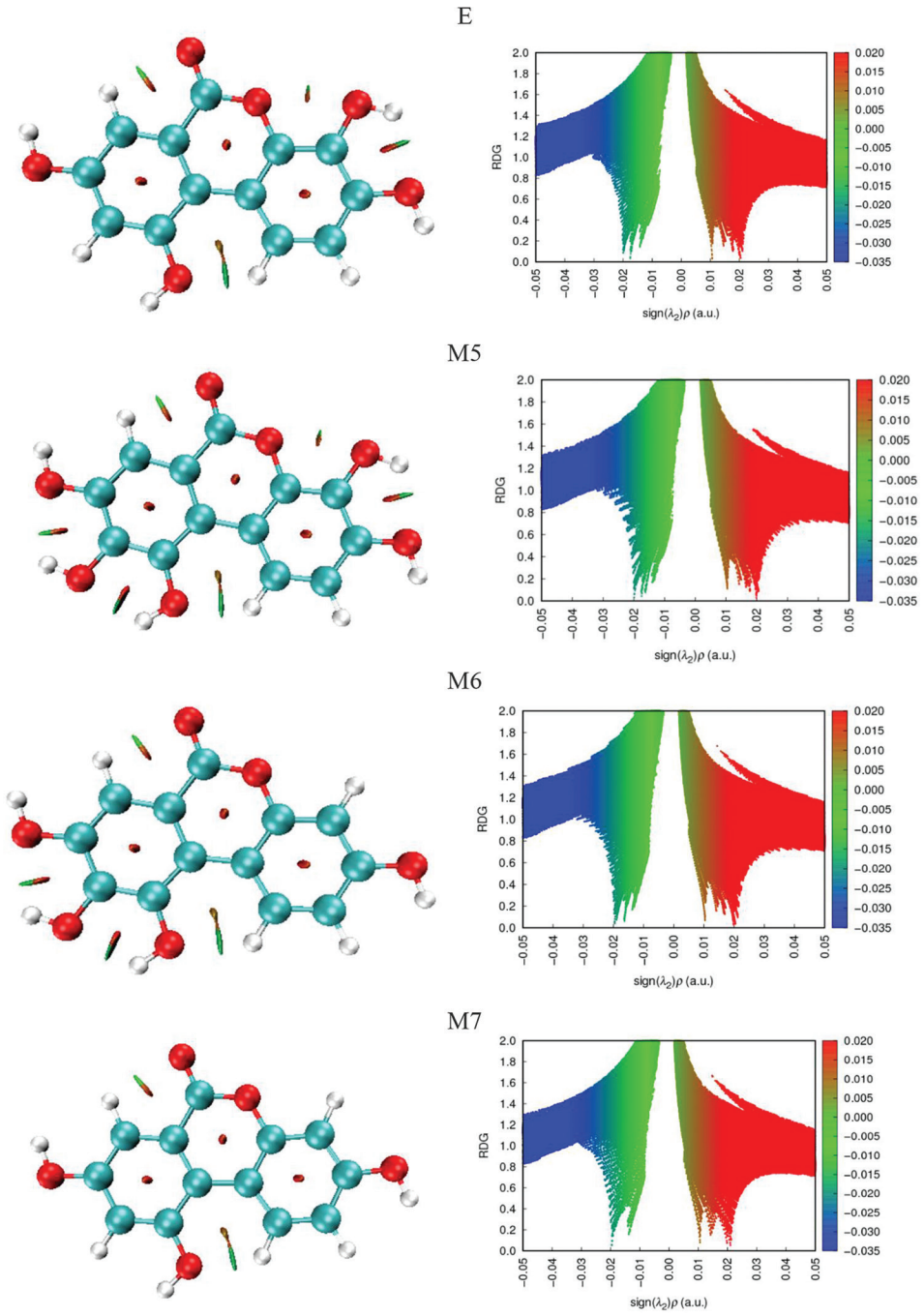

Fig. 2. Reduced density gradient and non-covalent interactions analysis for study compounds.

<12.0 kcal/mol. Medium hydrogen bonds have a positive second derivative of the electron density and a positive Hamiltonian, and an interaction energy between 12.0 and 24.0 kcal/mol. Strong hydrogen bonds have a negative electron density and a negative Hamiltonian, and an interaction energy >24.0 kcal/mol (Bader, 2010). According to Table I, all of the studied compounds have strong hydrogen-bonded interactions, except for Uro E, Uro M5, and Uro M6. Uro E has weak hydrogen-bonded interactions at O_2-H_{20}, Uro M5 has weak hydrogen-bonded interactions at O_3-H_{23} and O_2-H_{21}, and Uro M6 has weak hydrogen-bonded interactions at O_3-H_{24}, O_2-H_{21}, and O_2-H_{19}.

In conclusion, Uro E, Uro M5, Uro M6, and Uro M7 are all organic compounds that contain oxygen atoms. These atoms can form strong hydrogen bonds with the metal surface. When these compounds adsorb onto the metal surface, they form a layer that protects the metal from corrosion. Furthermore, Strong hydrogen bonds play a significant role in the topological parameters of a molecule and the corrosion inhibition efficiency of organic compounds. Compounds with strong hydrogen bonding interactions are more likely to form a strong bond with the metal surface and provide effective corrosion protection.

C. HOMO-LUMO

Comprehensive explanation of chemical reactivity characteristics such as HOMO-LUMO energy gap, chemical hardness, electronegativity, softness, chemical potential,

TABLE I
TOPOLOGICAL PARAMETERS (ALL IN A.U) AT THE BOND CRITICAL POINT (BCP) OF TITLE COMPOUND (ELECTRON DENSITY [ρ(r)], LAPLACIAN OF ELECTRON DENSITY [$\nabla^2 \rho$(r)], AND ELLIPTICITY [E]), THE UNITS OF V, G, AND H ARE IN A.U., AND HYDROGEN ENERGY (ε) (KCAL/MOL)

Bonds	$\rho(r)$	$\nabla^2 \rho(r)$	ε	V	G	H	E
Uro E							
O_2–H_{20}	0.020	0.085	0.012	−0.014	0.018	0.003	4.538
C_{16}–H_{22}	0.278	−0.940	0.027	−0.315	0.040	−0.275	98.822
C_{19}–H_{23}	0.278	−0.941	0.028	−0.317	0.041	−0.276	99.359
C_{15}–H_{21}	0.281	−0.965	0.026	−0.317	0.038	−0.279	99.408
C_{12}–H_{20}	0.290	−1.022	0.023	−0.330	0.038	−0.293	103.694
O_3–H_{25}	0.362	−2.549	0.021	−0.773	0.068	−0.705	242.599
O_2–H_{24}	0.366	−2.537	0.022	−0.775	0.071	−0.705	243.285
O_4–H_{26}	0.365	−2.542	0.022	−0.776	0.070	−0.706	243.348
O_5–H_{27}	0.365	−2.545	0.022	−0.776	0.070	−0.706	243.478
Uro M5							
O_3–H_{23}	0.020	0.097	2.031	−0.017	0.021	0.004	5.355
O_2–H_{21}	0.019	0.081	0.014	−0.014	0.017	0.003	4.323
O_4–H_{25}	0.363	−2.546	0.022	−0.774	0.069	−0.705	242.780
O_5–H_{26}	0.362	−2.548	0.022	−0.773	0.068	−0.705	242.609
C_{12}–H_{20}	0.281	−0.967	0.024	−0.316	0.037	−0.279	99.194
O_3–H_{24}	0.359	−2.545	0.021	−0.768	0.066	−0.702	240.922
C_{13}–H_{21}	0.290	−1.021	0.023	−0.330	0.037	−0.292	103.439
C_{18}–H_{22}	0.278	−0.941	0.028	−0.317	0.041	−0.276	99.364
O_2–H_{23}	0.360	−2.539	0.021	−0.769	0.067	−0.702	241.256
Uro M6							
O_3–H_{24}	0.020	0.096	2.817	−0.017	0.020	0.004	5.295
O_2–H_{21}	0.019	0.080	0.010	−0.013	0.017	0.003	4.232
C_{12}–H_{20}	0.281	−0.966	0.024	−0.316	0.037	−0.279	99.219
O_3–H_{25}	0.359	−2.545	0.021	−0.768	0.066	−0.702	240.909
C_{13}–H_{21}	0.290	−1.025	0.016	−0.329	0.036	−0.292	103.116
O_6–H_{27}	0.366	−2.539	0.022	−0.777	0.071	−0.706	243.822
O_2–H_{24}	0.360	−2.538	0.021	−0.769	0.067	−0.702	241.147
C_{17}–H_{22}	0.281	−0.968	0.027	−0.316	0.037	−0.279	99.195
C_{18}–H_{23}	0.278	−0.939	0.029	−0.317	0.041	−0.276	99.416
O_4–H_{26}	0.364	−2.546	0.022	–	–	–	–
Uro M7							
O_2–H_{19}	0.020	0.083	0.008	−0.014	0.017	0.003	4.433
O_3–H_{25}	0.365	−2.542	0.022	−0.776	0.070	−0.706	243.367
C_{15}–H_{22}	0.278	−0.941	0.027	−0.315	0.040	−0.275	98.799
C_{12}–H_{20}	0.281	−0.965	0.026	−0.317	0.038	−0.279	99.396
C_{11}–H_{19}	0.290	−1.026	0.017	−0.330	0.037	−0.293	103.392
C_{17}–H_{23}	0.278	−0.939	0.029	−0.317	0.041	−0.276	99.418
O_5–H_{26}	0.366	−2.539	0.022	−0.777	0.071	−0.706	243.753
O_2–H_{24}	0.365	−2.537	0.022	−0.775	0.071	−0.705	243.248
C_{14}–H_{21}	0.281	−0.968	0.027	−0.316	0.037	−0.279	99.195

electrophilicity, nucleophilicity, proton affinity, electrons transported from inhibitor to metal surface, electron-donating ability, and electron-donating ability. Determines the quantum chemical parameters of the compounds in both gas and aqueous phases, with a focus on Uro E, Uro M5, Uro M6, and Uro M7, as detailed in Tables II and III. The results confirm that all the analyzed molecules exhibit effective corrosion inhibition properties. The main objective of this theoretical research is to anticipate the corrosion inhibition performance of the substance and its derived compounds. Quantum chemical computations are useful for researching the link between molecule structure and corrosion inhibition efficacy. The smaller the HOMO energy, the harder it is to remove electrons from the molecular structure, and hence the more resistant to oxidation the compound, and have a greater potential to be excellent inhibitors. In general, there is a link between LUMO energy and inhibitory action. Compounds with high levels of LUMO energy are more probable to be excellent inhibitors because they can receive electrons from other compounds (Özbakır Işın, et al., 2020). The HOMO-LUMO bandgap identifies the compound's last electric charge contact and is useful in describing chemical electrical transport features. Low energy band gap (ΔE) values suggest that the material is particularly effective at inhibiting, and resisting corrosion in acidic environments. Adsorption techniques help by influencing the transport mechanism by the adsorbed layer, while the low-lying LUMO level induces chargeback donation from the metallic material to the chemical molecule. The energy of LUMO stability raises the corrosion inhibitor's electro-accepting capacity (Sujatha and Lavanya, 2023; Korkmaz, et al., 2022). According to research, increasing the bandgap (Uro E, Uro M5, Uro M6, Uro M7) raises corrosion while decreasing it improves the material's resilience to corrosion. This is due to the fact that just a little amount of energy is required to ionize and remove an electron from the last molecular-occupied orbitals. According to our findings, as shown in Tables II and III, the energy gap of protonated molecules is usually lower than that of neutral molecules in aqueous and pas phases, since protonation gives a positive charge to the compounds. In all, a molecule with a smaller energy gap is more polarizable, with more chemical activity and poorer kinetic stability. Overall, the reduction in band gap energy with protonation is an essential phenomenon with several possible uses, and it increases the material's corrosion resistance. Here, one of the applications of protonated is more polarizable (Mamad, et al., 2023b; Hekim, Azeez and Akpinar., 2019; Hssain, 2022).

As the electronegativity value lowers, the electron donor of excellent inhibitors to the metal surface enhances corrosion inhibition ability. In general, electronegativity is the capacity of a chemical species to attract the chemical electron density toward itself. In this study, the maximal electronegativity investigated the gas phase in protonated or (χ protonated > χ neutral). Small electronegativity readings represent that the chemical is a good corrosion inhibitor, anti-corrosion inhibitor protonated < anti-corrosion inhibitor neutral. Here, electronegativity is the capacity of a chemical species to attract in protonated greater than neutral. The above data indicates that compounds with a high electronegativity value can't be used as useful corrosion inhibitors (Özbakır Işın, et al., 2020; Qader, et al., 2019; Yousif and Hanaa, 2021b).

Rises in inhibitory performance are inversely related to drops in electronegativity values because the inhibitor's atoms' ability to attract electrons decreases (Razali, et al., 2023). Hard compounds contain larger energy gaps, making them more chemical stable and less chemical reactive. Soft chemical compounds are more reactive than hard compounds because they can more readily donate electrons to an acceptor. According to energy gaps (Fig. 4), chemical stability, and reactiveness, the corrosion inhibition efficiency is ranked from highest to lowest: (Uro M6 > Uro M5 > Uro M7 > Uro E) using protonated/gas phase. Improving chemical hardness may be beneficial to corrosion resistance. As a result, the (Uro E) compound inhibitor that had higher ELUMO (-3.44 eV) and low energy gap (3.031 eV) was shown to have high softness (0.330 eV-1), and low hardness (1.516 eV) scores in the gas phase/protonated technique. This data indicate that the Uro E compound has a high kinetic no stability and a high molecular reactivity. Nucleophilicity and electrophilicity are theoretical chemistry characteristics that may be used to predict the chemical behavior of compounds,

http://dx.doi.org/10.14500/aro.11828

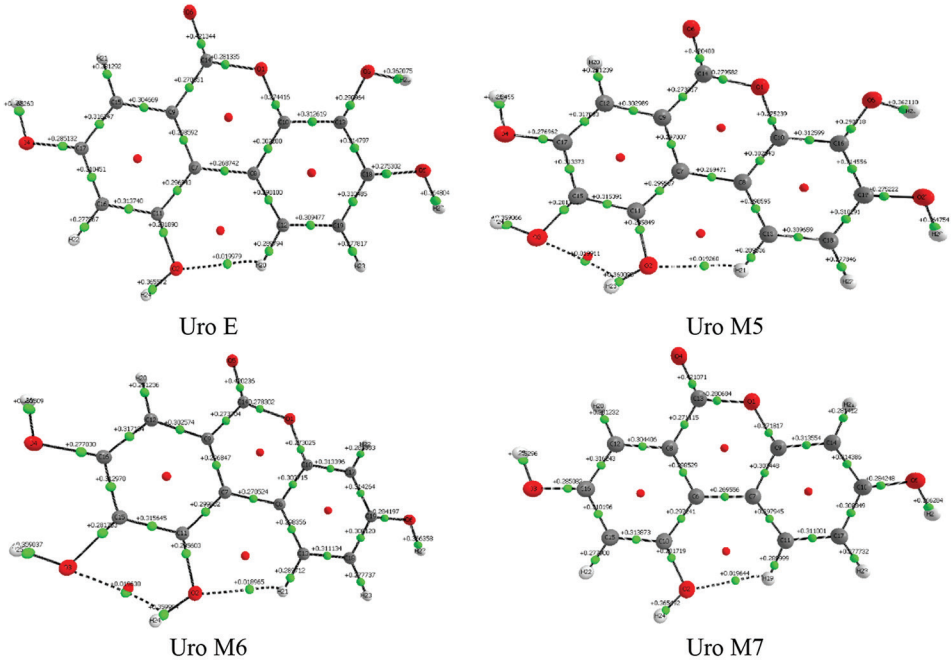

Fig. 3. Graph representation of neutral molecular state.

TABLE II
QUANTUM CHEMICAL PARAMETERS FOR COMPOUND AT GAS PHASE

Neutral					Protonated			
Parameters	Uro E	Uro M5	Uro M6	Uro M7	Uro E	Uro M5	Uro M6	Uro M7
HOMO (eV)	−5.957	−5.978	−6.014	−5.986	−9.513	−9.446	−9.686	−9.734
LUMO (eV)	−1.871	−1.647	−1.707	−1.927	−6.671	−6.405	−6.473	−6.741
Ionization energy (eV)	5.957	5.978	6.014	5.986	9.513	9.446	9.686	9.734
Electron Affinity (eV)	1.871	1.647	1.707	1.927	6.671	6.405	6.473	6.741
Energy gap (eV)	4.086	4.331	4.307	4.059	2.842	3.041	3.213	2.993
Hardness (eV)	2.043	2.166	2.154	2.030	1.421	1.521	1.607	1.497
Softness (eV)-1	0.245	0.231	0.232	0.246	0.352	0.329	0.311	0.334
Electronegativity (eV)	3.914	3.813	3.861	3.957	8.092	7.926	8.080	8.238
Chemical potential (eV)	−3.914	−3.813	−3.861	−3.957	−8.092	−7.926	−8.080	−8.238
Electrophilicity (eV)	3.749	3.356	3.460	3.857	23.040	20.656	20.317	22.672
Nucleophilicity (eV)-1	0.267	0.298	0.289	0.259	0.043	0.048	0.049	0.044
Back-donation (eV)	−0.511	−0.541	−0.538	−0.507	−0.355	−0.380	−0.402	−0.374
Electron transfer ΔN	1.916	1.761	1.793	1.949	5.695	5.212	5.029	5.505

TABLE III
QUANTUM CHEMICAL PARAMETERS FOR COMPOUND AT AQUEOUS PHASE

Parameters	Neutral				Protonated			
	Uro E	Uro M5	Uro M6	Uro M7	Uro E	Uro M5	Uro M6	Uro M7
HOMO (eV)	−5.981	−6.027	−6.053	−6.147	−6.471	−6.501	−6.620	−6.576
LUMO (eV)	−2.093	−1.866	−1.867	−2.053	−3.440	−3.230	−3.255	−3.432
Ionization energy (eV)	5.981	6.027	6.053	6.147	6.471	6.501	6.620	6.576
Electron Affinity (eV)	2.093	1.866	1.867	2.053	3.440	3.230	3.255	3.432
Energy gap (eV)	3.888	4.161	4.186	4.094	3.031	3.271	3.365	3.144
Hardness (eV)	1.944	2.081	2.093	2.047	1.516	1.636	1.683	1.572
Softness (eV)-1	0.257	0.240	0.239	0.244	0.330	0.306	0.297	0.318
Electronegativity (eV)	4.037	3.947	3.960	4.100	4.956	4.866	4.938	5.004
Chemical potential (eV)	−4.037	−3.947	−3.960	−4.100	−4.956	−4.866	−4.938	−5.004
Electrophilicity (eV)	4.192	3.743	3.746	4.106	8.102	7.237	7.245	7.964
Nucleophilicity (eV)-1	0.239	0.267	0.267	0.244	0.123	0.138	0.138	0.126
Back-donation (eV)	−0.486	−0.520	−0.523	−0.512	−0.379	−0.409	−0.421	−0.393
Electron transfer	2.077	1.897	1.892	2.003	3.270	2.975	2.935	3.183

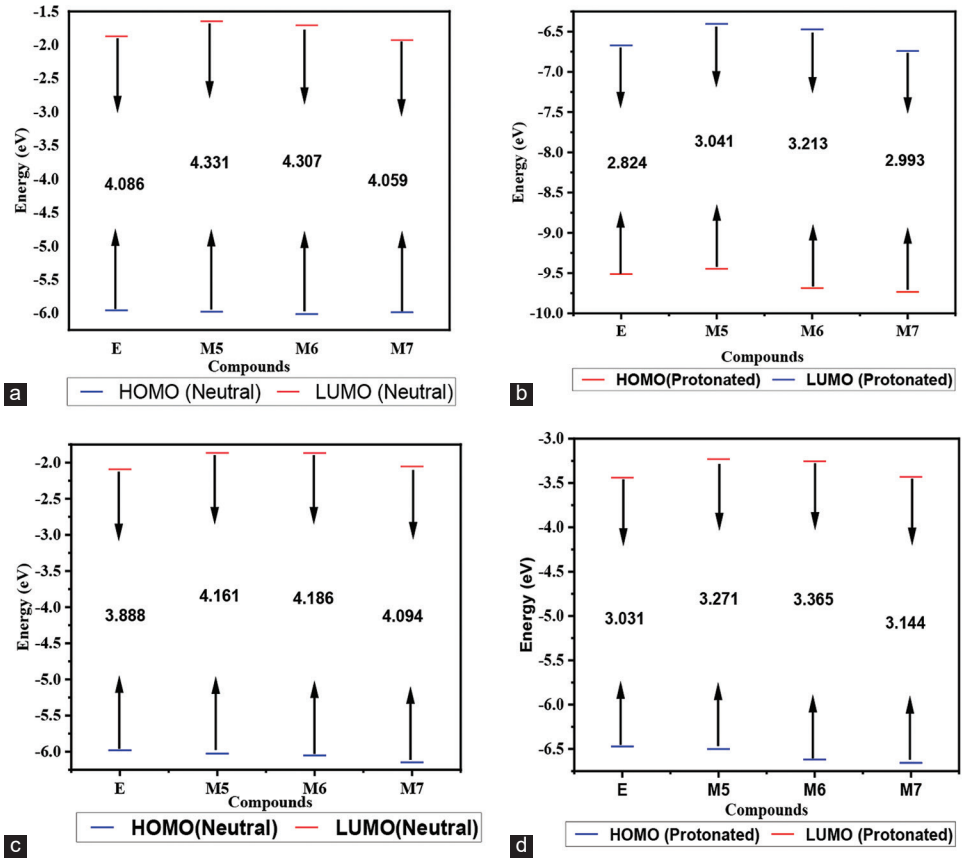

Fig. 4. Energy bandgap for all compounds (a) Neutral gas phase (b) Protonated gas phase (c) Neutral aqueous phase (d) Protonated aqueous phase.

and these values reflect their efficacy. It is vital to note that a molecular structure with a high nucleophilic value may effectively suppress corrosion inhibitors. In contrast, a material with a high electrophilic value provides no corrosion protection benefit. Nucleophiles are compounds that transfer an electron pair to form a connection with another chemical species, while electrophiles are electron-deficient compounds. The predicted ranking of corrosion inhibition effectiveness may be constructed by taking into account the nucleophilic and electrophilic values of the compounds investigated: Uro E > Uro M7 > Uro M5 > Uro M6 using the protonated method (Caid, et al., 2023). The electron transfer has an inverse relationship with the energy gap, implying that a greater value equates to a stronger corrosion inhibition capacity. According to the aqueous, and gas phases, the Uro E compound has the greatest electron transfer value, suggesting a large potential for electron release in the metals using neutral/protonated methods. The faster the electron transfer rate, the more probable corrosion will develop. Whenever the back donation of energy from a molecular structure to a metal is favored, it indicates that the inhibitor has a positive hardness and a negative back donation energy. The physical, and chemical interaction that occurs between inhibitors and the metal surfaces is influenced by the back-donation mechanism. According to this hypothesis, if back-donation from a molecule and electron transfer to the molecule happens simultaneously, the energy shift is proportional to the hardness of the molecules. The chemical contact between the molecule that inhibits and its chemical surface may be influenced by an electrical back-donation mechanism. When back-donation is < zero, or η > zero, The transfer of electrons from the molecular structure to the metal is favorable in terms of energy. The computed back-donation numbers in this study show a trend: ΔE b – d aqueous > ΔE b – d gas phase, because molecules of water are present in the aqueous technique (Qadr and Mamand, 2023). The protonated state has a negative influence on BG energy. Chemical stability, a change in the material's corrosion behavior, and peculiar corrosion inhibition difficulties are all directly tied to BG energy. Overall, increasing ionization energy, electron affinity, softness, and reducing the energy band gap may all increase corrosion resistance and inhibition. Protonated chemicals may be utilized to create coatings, inhibitors, and self-healing materials that protect metals against corrosion in a range of conditions.

D. MEP

Fig. 5 also depicts the MEP of (Uro E, Uro M5, Uro M6, Uro M7) compounds using the gas phase. The MEP is a useful tool for identifying the relative polarity of a molecular structure and whether or not certain regions in it have proton affinity or charge-regulated hard-hard interactions. The potential energy map (PEM) is a critical component in characterizing the arrangement of structural elements on a compound's surface. In color, PEM depicts the electrostatic potential surrounding a molecular structure. The electrostatic potential (ESP) Map may be affected by factors such as increased electron affinity, dipole moment, quantity of ionization, electronegativity, and electron density (Yıldız, et al., 2023). Increased ionization energy, electron affinity, softness, and a smaller energy band gap may all cause the (MEP) to become red. When electronegativity is high, an area of a molecule's electrostatic potential map becomes blue.

http://dx.doi.org/10.14500/aro.11828

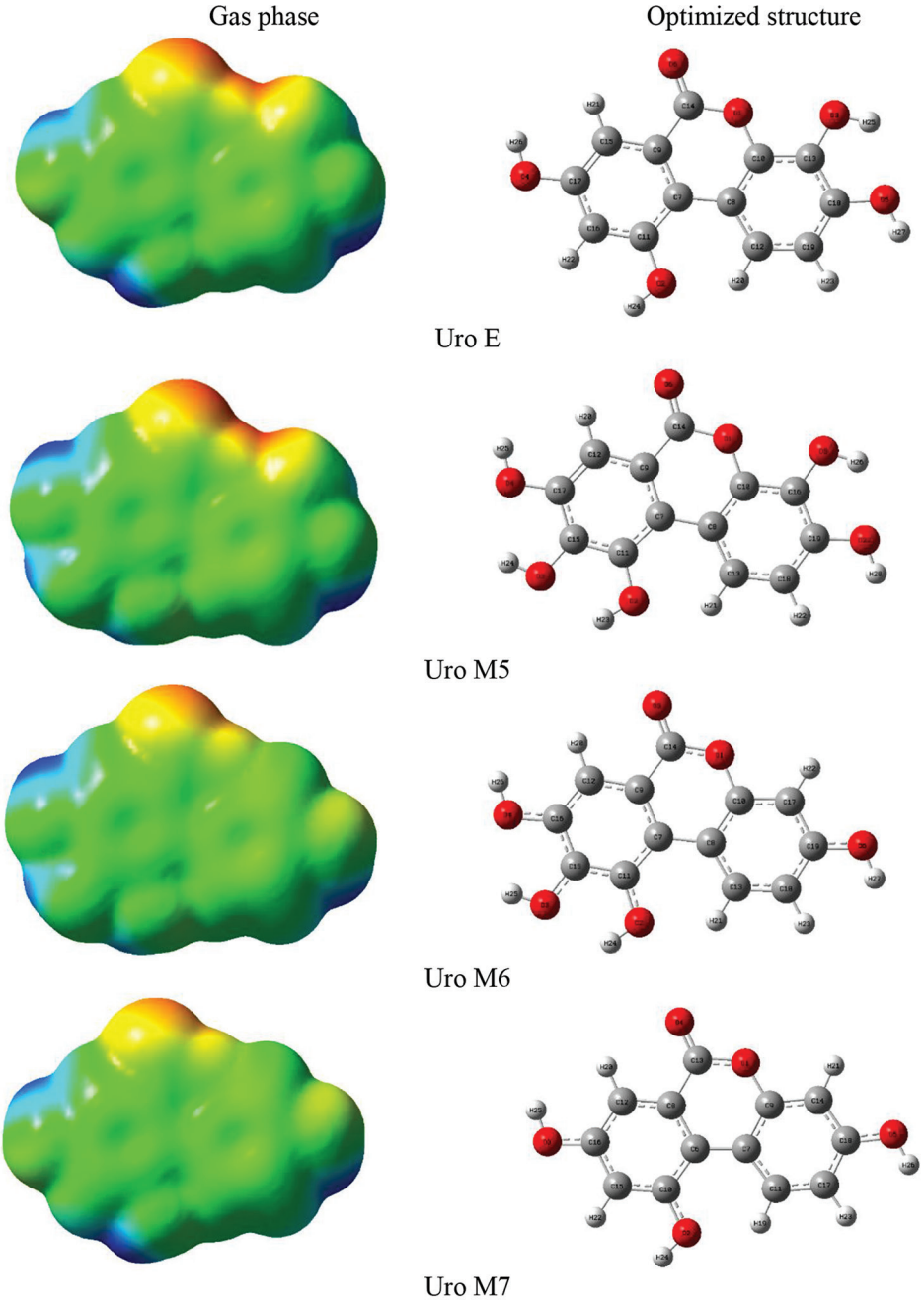

Fig. 5. Optimized molecular geometries and molecular electrostatic potential maps for all compounds.

Blue areas are more positively charged, have a lower electron density, and have a lower affinity for a proton. The existence of a red zone in a MEP map may be a strong predictor of corrosion resistance. Increase Positive charge (protonated) attracts electrons, which may aid in the formation of a protective layer on a metal's surface. Overall, the blue zone in a MEP map is a flexible tool for designing novel materials and catalysts with enhanced capabilities, as well as a strong instrument for advancing a broad variety of scientific subjects (Akman, et al., 2023; Mustafa and Mohammad, 2023).

E. Thermal Properties

The key thermodynamic parameters, enthalpy (ΔH), entropy (ΔS), Gibbs free energy (ΔG), and heat capacity (Cv) were computed for the investigated compounds using DFT with the 6-311++G(d,p) basis set. Calculations were performed in the gas phase at temperatures ranging from 100 K to 1000 K. Notably, the temperature dependence significantly affects the thermodynamic properties of the studied compounds (Arulaabaranam, et al., 2021; Fayomi, et al., 2021; Merdas, 2021). Our analysis using DFT revealed a consistent trend across all investigated compounds (E, M5, M6, and M7). As temperature increases from 25 K to 1000 K, most thermodynamic functions (enthalpy, entropy, and heat capacity) exhibit a positive correlation, indicating a rise in their values (Fig. 6). This behavior aligns with expectations as higher temperatures generally lead to increased molecular vibrations. However, Gibbs free energy (ΔG) shows an opposing trend, becoming increasingly negative with rising temperature. The positive enthalpy change (ΔH) observed throughout

the temperature range signifies that the dissolution process for these molecules is endothermic, requiring an energy input (Abbaz, Bendjeddou and Villemin, 2018; Srivastavaa, et al., 2019; Yousif and Hanaa, 2021a). This suggests that dissolving these compounds is not a spontaneous process under the studied conditions. Increasing temperature may cause a change in the adsorption behavior of inhibitor molecules on metal surfaces, as shown by the trend in

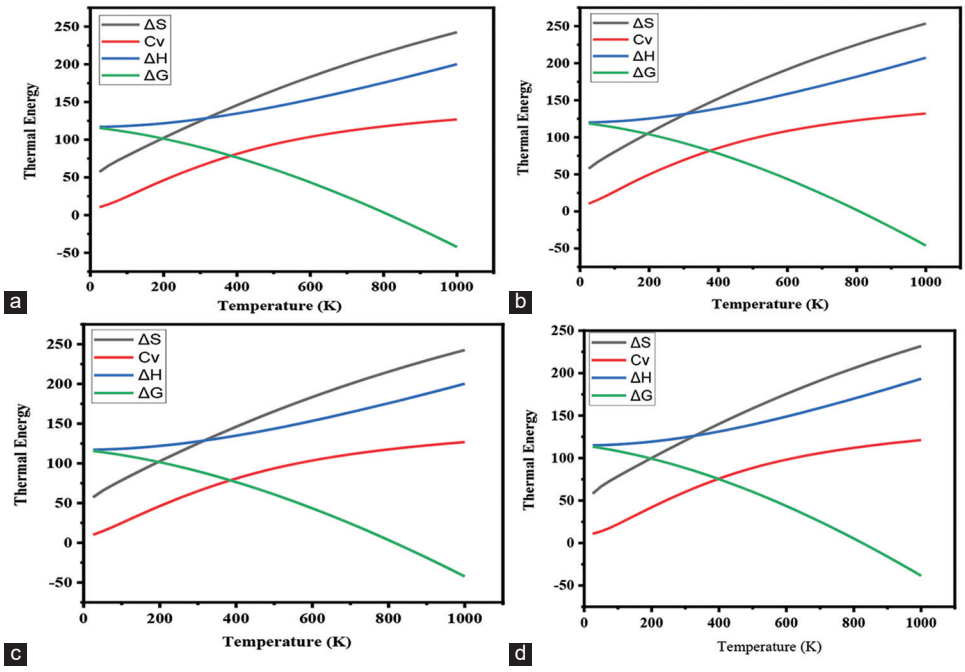

Fig. 6. Thermal properties for, (a) E compound, (b) M5 compound, (c) M6 compound, and (d) M7 compound.

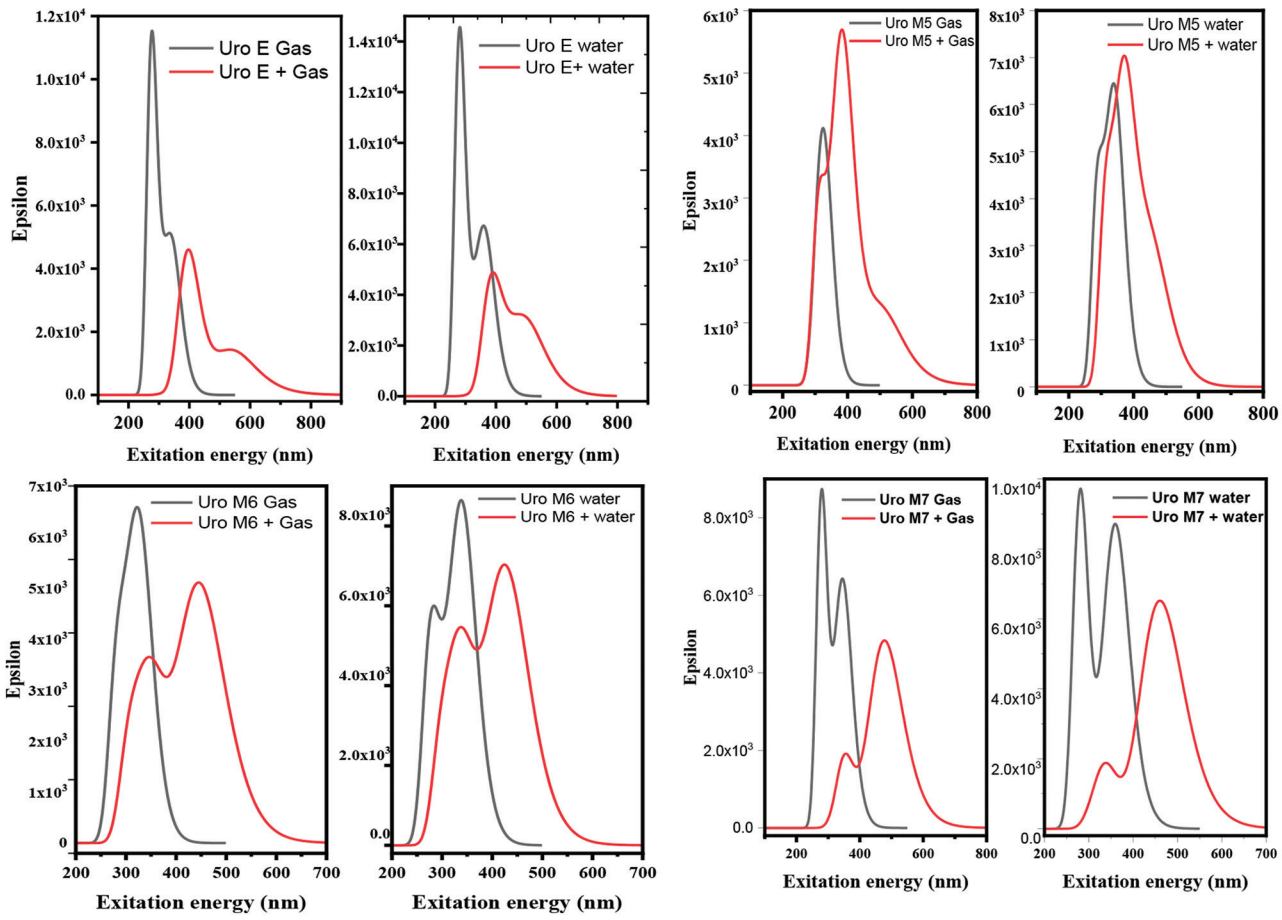

Fig. 7. Ultraviolet-visible analysis for all compounds in gas and aqueous phase.

http://dx.doi.org/10.14500/aro.11828

TABLE IV
FUKUI FUNCTIONS AT THE GAS PHASE

Atoms	Uro E			Uro M5			
	f_k^-	f_k^+	Δf	Atoms	f_k^-	f_k^+	Δf
O (1)	0.016	0.041	0.025	O (1)	0.015	0.04	0.025
O (2)	0.022	0.028	0.006	O (2)	0.021	0.028	0.007
O (3)	0.068	0.021	−0.047	O (3)	0.027	0.048	0.021
O (4)	0.062	0.043	−0.019	O (4)	0.049	0.034	−0.015
O (5)	0.073	0.03	−0.043	O (5)	0.077	0.023	−0.054
O (6)	0.058	0.108	0.05	O (6)	0.057	0.106	0.049
C (7)	0.018	0.05	0.032	C (7)	0.013	0.054	0.041
C (8)	0.031	0.002	−0.029	C (8)	0.032	0.000	−0.032
C (9)	0.018	0.039	0.021	C (9)	0.019	0.035	0.016
C (10)	0.026	0.002	−0.024	C (10)	0.028	0.005	−0.023
C (11)	0.03	0.022	−0.008	C (11)	0.03	0.02	−0.010
C (12)	0.045	0.017	−0.028	C (12)	0.033	0.046	0.013
C (13)	0.037	0.027	−0.01	C (13)	0.05	0.022	−0.028
C (14)	0.017	0.083	0.066	C (14)	0.015	0.081	0.066
C (15)	0.04	0.049	0.009	C (15)	0.025	0.079	0.054
C (16)	0.021	0.083	0.062	C (16)	0.04	0.029	−0.011
C (17)	0.031	0.02	−0.011	C (17)	0.037	0.025	−0.012
C (18)	0.056	0.031	−0.025	C (18)	0.022	0.02	−0.002
C (19)	0.022	0.02	−0.002	C (19)	0.058	0.033	−0.025
H (20)	0.049	0.031	−0.018	H (20)	0.043	0.053	0.010
H (21)	0.046	0.054	0.008	H (21)	0.051	0.032	−0.019
H (22)	0.048	0.066	0.018	H (22)	0.061	0.047	−0.014
H (23)	0.059	0.046	−0.013	H (23)	0.024	0.023	−0.001
H (24)	0.027	0.025	−0.002	H (24)	0.018	0.026	0.008
H (25)	0.024	0.02	−0.004	H (25)	0.022	0.022	0.000
H (26)	0.024	0.022	−0.002	H (26)	0.026	0.02	−0.006
H (27)	0.032	0.02	−0.012	O (27)	0.075	0.031	−0.044
				H (28)	0.033	0.02	−0.013

TABLE V
FUKUI FUNCTIONS AT THE GAS PHASE

Atoms	Uro M6			Uro M7			
	f-	f+	Δf	Atoms	f-	f+	Δf
O (1)	0.024	0.036	0.012	O (1)	0.026	0.041	0.015
O (2)	0.033	0.024	−0.009	O (2)	0.031	0.027	−0.004
O (3)	0.028	0.045	0.017	O (3)	0.069	0.043	−0.026
O (4)	0.052	0.032	−0.02	O (4)	0.068	0.109	0.041
O (5)	0.067	0.103	0.036	O (5)	0.078	0.037	−0.041
O (6)	0.077	0.036	−0.041	C (6)	0.025	0.051	0.026
C (7)	0.022	0.055	0.033	C (7)	0.038	0.00	−0.038
C (8)	0.045	−0.001	−0.046	C (8)	0.017	0.037	0.02
C (9)	0.019	0.037	0.018	C (9)	0.026	0.00	−0.026
C (10)	0.029	0.005	−0.024	C (10)	0.034	0.021	−0.013
C (11)	0.038	0.021	−0.017	C (11)	0.021	0.021	0.00
C (12)	0.04	0.043	0.003	C (12)	0.047	0.048	0.001
C (13)	0.02	0.026	0.006	C (13)	0.021	0.084	0.063
C (14)	0.024	0.09	0.066	C (14)	0.032	0.024	−0.008
C (15)	0.027	0.08	0.053	C (15)	0.023	0.083	0.06
C (16)	0.044	0.026	−0.018	C (16)	0.033	0.019	−0.014
C (17)	0.03	0.024	−0.006	C (17)	0.037	0.021	−0.016
C (18)	0.039	0.02	−0.019	C (18)	0.035	0.026	−0.009
C (19)	0.04	0.03	−0.01	H (19)	0.042	0.032	−0.01
H (20)	0.048	0.052	0.004	H (20)	0.05	0.054	0.004
H (21)	0.042	0.034	−0.008	H (21)	0.053	0.041	−0.012
H (22)	0.053	0.043	−0.01	H (22)	0.052	0.066	0.014
H (23)	0.06	0.049	−0.011	H (23)	0.059	0.048	−0.011
H (24)	0.025	0.023	−0.002	H (24)	0.028	0.025	−0.003
H (25)	0.02	0.026	0.006	H (25)	0.026	0.022	−0.004
H (26)	0.024	0.022	−0.002	H (26)	0.029	0.02	−0.009
H (27)	0.03	0.021	−0.009				

ΔG. As seen in Fig. 6, the observed positive ΔH values at lower temperatures align with endothermic physisorption, a weaker type of adsorption. Increasingly negative ΔG values at higher temperatures indicate chemisorption potential. Thermal energy may assist this transition by activating inhibitor molecules and metal surfaces to generate stronger chemical interactions. Since chemisorption protects against corrosion better than physisorption, this shift is essential for developing corrosion inhibitors. Thermal characteristics (Gibbs free energy), If the temperature rises from 825 to 1000 Kilven, all chemicals on the metal surface may chemisorption.

F. Ultraviolet (UV)-Visible Spectroscopy

UV spectroscopy is often used for quantitative and qualitative chemical analysis, as well as structural characterization (Salih, et al., 2023). The computed absorption spectrum shows that the maximum absorption wavelength corresponds to the transition of electrons from HOMO, LUMO. According bellow Fig. 7, the Gas phase and water solvent have been used to investigate the UV-visible of (Uro M6 > Uro M5 > Uro M7 > Uro E) compounds. The link between absorbance and corrosion resistance is complicated. In general, substances with a high absorbance are more prone to corrosion, while those with a low absorbance are able to resist corrosion. For evaluating the accuracy of peak location in the calculation of UV-visible wavelengths, the kind of basis set, and solvent is more important than the number of peaks. The greatest absorption wavelength parallels the chemical electronic shift from HOMO to LUMO molecular orbital, according to shifting and the absorption spectrum. The impact of neutral and protonated clearly has been studied based on peak location in the UV-visible, as illustrated in Fig. 7. When Uro E to M7 molecules are changed from neutral to protonated, their absorption of UV peak rises, as a result, increase positive charge (protonated).

G. Fukui functions

The Fukui Function gives information on the reactivity indices in a given system. For the highest Fukui function values, the atom exhibits a significant degree of reactivity. The Fukui functions from (Uro M6 > Uro M5 > Uro M7 > Uro E) have been calculated on the basis of B3LYP/6-311G++(d, p) level of theory, and the results are shown in Tables IV and V. The Fukui Functions ($f_k^-, f_k^+ f_k^0$) are computed using Mulliken population analysis charges of neutral, negative, and positive ions using equation (12-14). If (N) represents the number of electrons, then (N + 1) denotes an ion and (N – 1) denotes the system's cation (Caid, et al., 2023; Razali, et al., 2023).

$$f_k^+ = q(N+1) - q(N) \tag{12}$$

$$f_k^- = q(N) - q(N-1) \tag{13}$$

$$f_k^- \tag{14}$$

Furthermore, The Fukui function is a valuable tool for understanding the reactivity of molecules in corrosion inhibition. It helps identify regions within the inhibitor

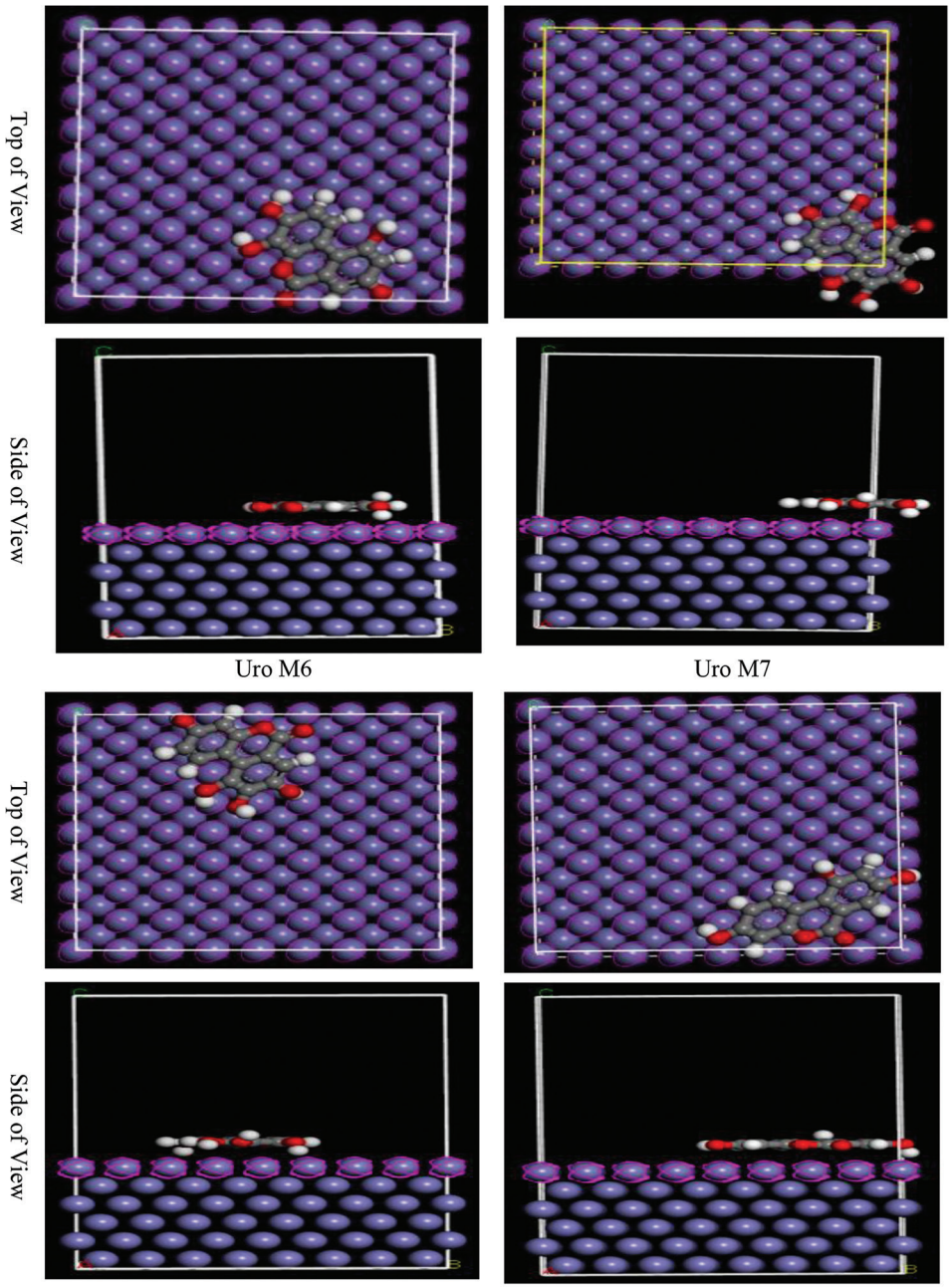

Fig. 8. The low-energy configurations for the adsorption of neutral forms of the study compounds on the Fe(110) surface were determined using Monte Carlo simulations.

molecule with enhanced electrophilic character (f_k^+). These regions, characterized by a higher Fukui function value, are more susceptible to attack by electron-rich species (nucleophiles). Conversely, the most nucleophilic atoms within the inhibitor molecule will exhibit the highest Fukui function value (f_k^-). During adsorption on a metal surface, the inhibitor molecule interacts with the metal through electron transfer. This electron transfer process influences the electronic density at both the nucleophilic and electrophilic sites on the inhibitor molecule. Therefore, the Fukui function analysis provides valuable insights into the potential adsorption sites on the metal surface. It essentially helps pinpoint which areas of the inhibitor molecule are more likely to interact and form bonds with the metal, ultimately determining the reactive sites during the adsorption process (Caid, et al., 2023; Fan, et al., 2022; Razali, et al., 2023). The condensed Fukui function serves as a helpful indicator of nucleophilic character within a molecule. Sites with a positive Fukui function ($\Delta f > 0$) are considered electrophilic, while those with a negative value ($\Delta f < 0$) are considered nucleophilic. Our analysis revealed that several atoms in the investigated compounds (Uro M6, Uro M5, Uro M7, and Uro E) exhibit significant nucleophilic character as shown in Table IV and V. Among the oxygen atoms analyzed, Uro M7 (O4) displayed the strongest nucleophilicity ((f_k^-) = 0.109), followed by Uro E (O6) ((f_k^-) = 0.108), Uro M5 (O6) ((f_k^-)= 0.106), and Uro M6 (O5) (f_k^-)= 0.103). This trend suggests that oxygen atoms within these molecules are generally more susceptible to nucleophilic attack compared

http://dx.doi.org/10.14500/aro.11828

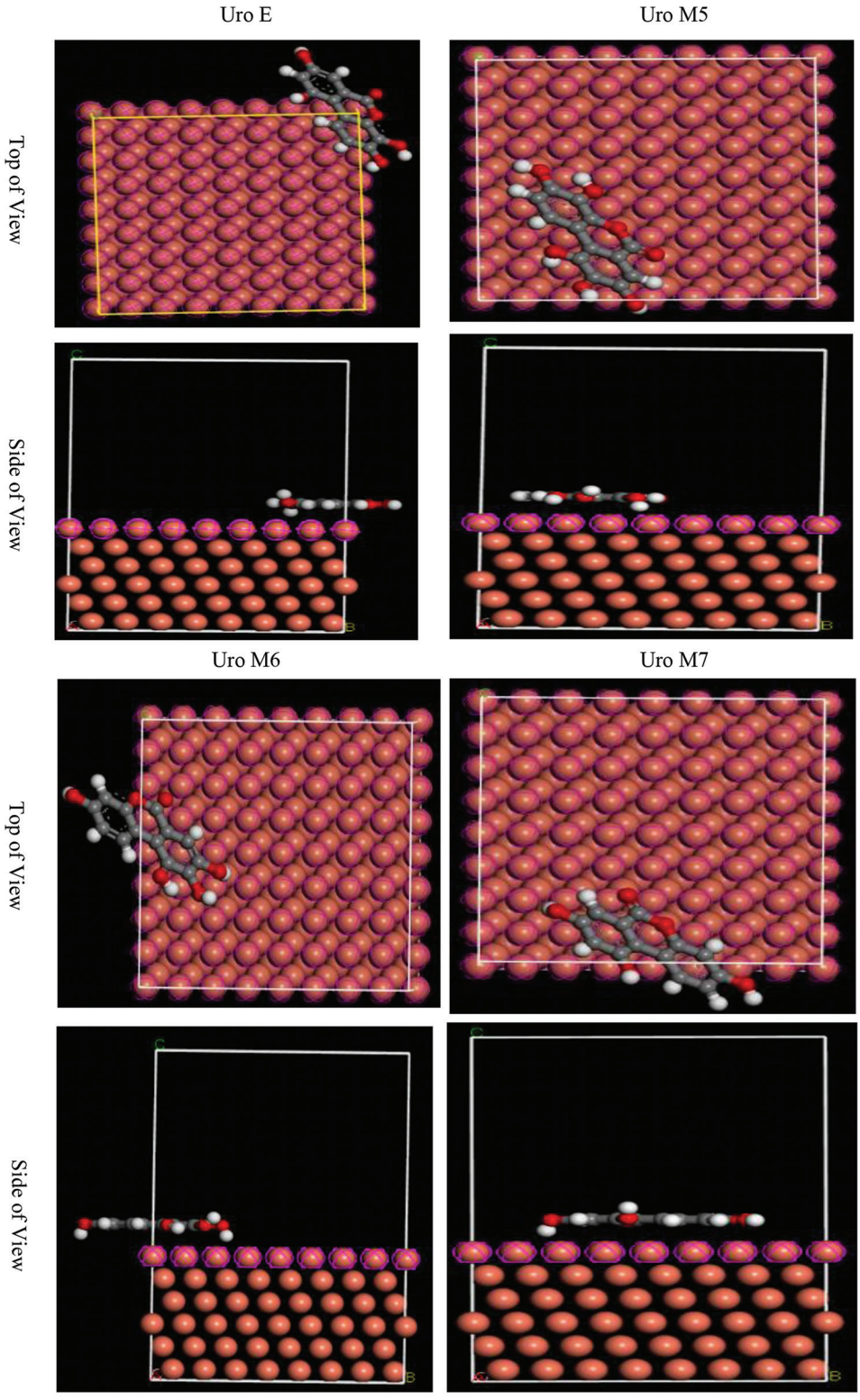

Fig. 9. The low-energy configurations for the adsorption of neutral forms of the study compounds on the Cu(111) surface were determined using Monte Carlo simulations.

to carbon and hydrogen atoms. The higher electronegativity (O: 3.44 > C: 2.55 > H: 2.20) and electron affinity of oxygen atoms contribute to their vulnerability toward nucleophiles. Oxygen's inherent ability to attract electrons (electronegativity) and its tendency to gain additional electrons (electron affinity) make it a more favorable target for nucleophilic attack compared to carbon and hydrogen.

H. Monte Carlo Simulation

The investigation of the adsorption of Uor E, Uor M5, Uor M6, and Uor M7 on metal surfaces Fe (110), Cu (111), and Al (111) was conducted using Monte Carlo simulations in the gas phase. These simulations were performed using the Adsorption Locator module of the Material Studio program. The computational methodology used for the implementation

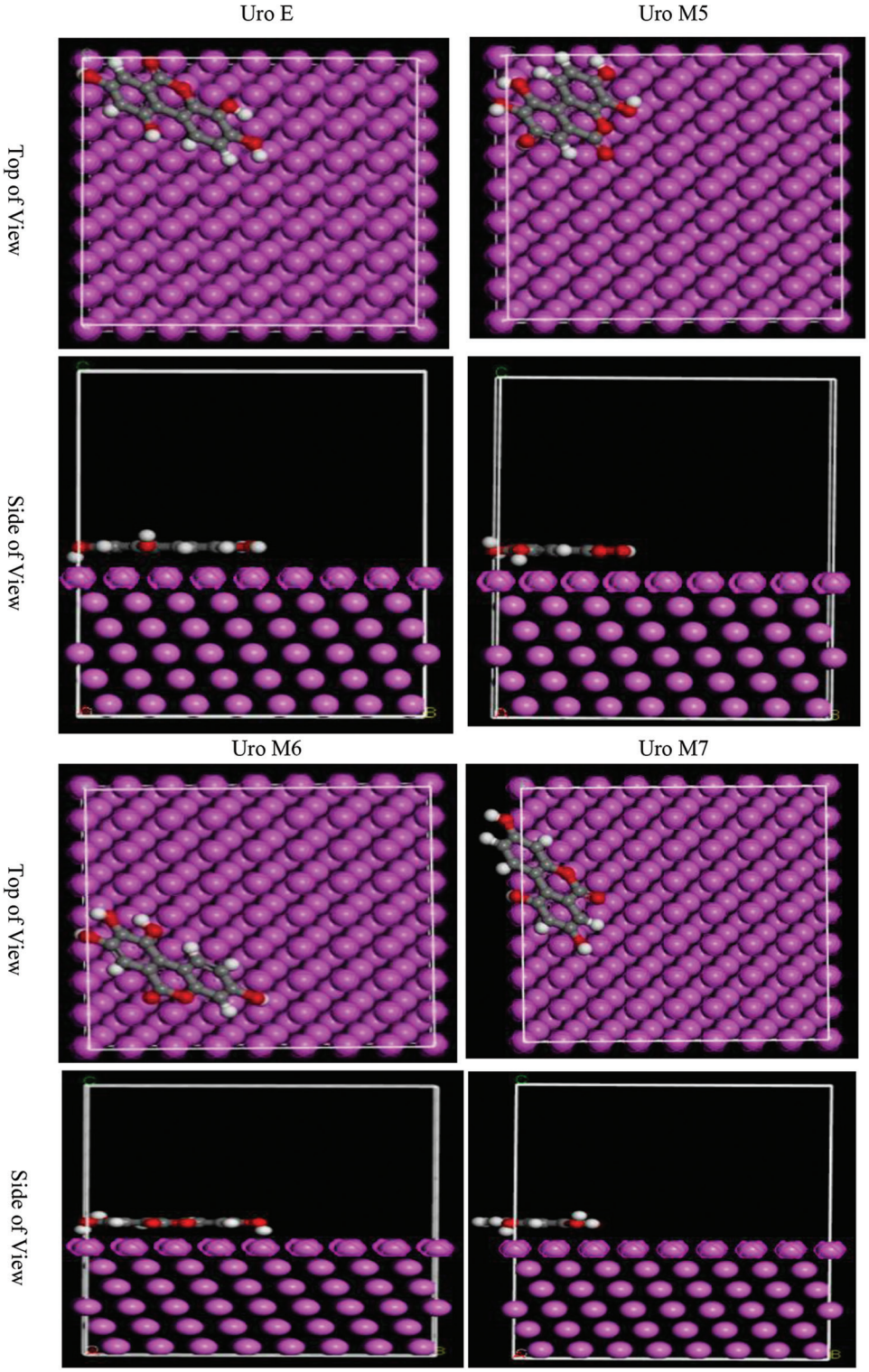

Fig. 10. The low-energy configurations for the adsorption of neutral forms of the study compounds on the Al(111) surface were determined using Monte Carlo simulations.

of the model has been founded upon the Metropolis algorithm (Metropolis, et al., 1953; Mamad, Omer and Othman, 2023a, Hamad, et al., 2025). Monte Carlo simulations use simulated annealing with 50,000 steps in each iteration. Energy calculations and equilibrium configuration searches were carried out using the condensed phase optimized molecular potentials for atomistic simulation studies (COMPASSIII) force field. The Ewald approach was used to characterize electrostatic interactions with a precision of 1×10^{-5} kcal/mol (Sun, Ren and Fried, 1998; Sun, Ren and Fried, 1998). The calculation of van der Waals interaction energy was performed using the Atom-based approach. Non-bond interactions were subjected to a cubic spline truncation with a cutoff distance of 18.5 Å (Mamand, Azeez and Qadr,

http://dx.doi.org/10.14500/aro.11828

2023). Monte Carlo simulations are used to forecast the manner in which inhibitor molecules interact with the metal surface. These Monte Carlo simulation data for outputs and descriptors are provided in Table VI. The parameters of the substrate-adsorbate configuration include the total energy, which is the sum of the energies of the adsorbate components, rigid adsorption energy, and deformation energy. Adsorption energy measures the energy generated or needed to adsorb the relaxed adsorbate component onto the substrate. The adsorption energy is the sum of the rigidity and deformation energies for the adsorbate component. The rigid adsorption energy measures the energy generated or required for adsorbing the unrelaxed adsorbate component on the substrate before geometry adjustment. The deformation energy measures the energy released when the adsorbate component relaxes on the substrate surface. Finally, (dEad/dNi) shows the energy of substrate-adsorbate combinations with one adsorbate component removed. This study investigated the adsorption behavior of urolithin derivatives (Uor E, Uor M5, Uor M6, and Uor M7) on iron (Fe(110)), copper (Cu(111)), and aluminum (Al(111)) surfaces using MC simulations as can be seen in Figs. 8-10. Adsorption energies were decomposed into van der Waals, electrostatic, and intramolecular components (results not shown). All energies were negative, signifying a spontaneous adsorption process. The primary goal was to identify the most stable adsorption configurations for each molecule on the chosen metal surfaces, known for their stability. Analysis of Table VI reveals a trend in the negative adsorption energies (indicating stronger adsorption) across the three surfaces: Uor M5 > Uor M6 > Uor E > Uor M7. This suggests that Uor M5 exhibits the most favorable adsorption characteristics, implying superior stability and a stronger affinity for metal surfaces compared to the other urolithin derivatives.

TABLE VI
The Outputs and Descriptors Calculated by the Monte Carlo Simulation for Adsorption of Uroe, Urom5, Urom6, And Urom7 Inhibitors on fe (110), Cu (111), And Al (111) (In Kcal Mol^{-1})

Fe (110)					
Inhibitor	Total energy	Adsorption energy	Rigid adsorption	Deformation energy	$\frac{dE_{ad}}{dN_i}$
Uro E	-166.725	-135.306	-136.056	0.750011	-135.306
Uro M5	-149.344	-140.133	-140.681	0.547236	-140.133
Uro M6	-156.143	-138.493	-138.978	0.485144	-138.493
Uro M7	-180.884	-130.711	-131.518	0.806903	-130.711
Cu (111)					
Uro E	-104.649	-73.2292	-73.6061	0.376818	-73.2292
Uro M5	-85.1371	-75.9262	-76.1607	0.234514	-75.9262
Uro M6	-92.495	-74.8441	-75.0469	0.202769	-74.8441
Uro M7	-120.865	-70.6923	-71.012	0.319699	-70.6923
Al (111)					
Uro E	-99.3766	-67.9572	-68.257	0.299823	-67.9572
Uro M5	-79.7369	-70.526	-70.6891	0.163137	-70.526
Uro M6	-87.116	-69.4651	-69.6028	0.137712	-69.4651
Uro M7	-115.865	-65.692	-65.9318	0.23977	-65.692
Ni (111)					
Uro E	-115.326	-83.9067	-84.3779	0.471165	-83.9067
Uro M5	-96.0763	-86.8654	-87.1986	0.333158	-86.8654
Uro M6	-102.818	-85.1675	-85.5571	0.389566	-85.1675
Uro M7	-131.126	-80.9528	-81.3577	0.404844	-80.9528

IV. Conclusion

This study explores the potential of four urolithin derivatives (Uro E, Uro M5, Uro M6, and Uro M7) as corrosion inhibitors using quantum chemical calculations. The investigation aimed to identify relationships between various molecular properties and their predicted corrosion inhibition effectiveness. Our findings suggest that increasing ionization energy, electron affinity, and softness while decreasing the energy band gap and electronegativity could enhance corrosion resistance. Protonation appears to be a promising strategy, with Uro E exhibiting the highest predicted efficacy based on nucleophilic and electrophilic characteristics. Lower ω and higher ε values for Uro E further support its potential for electron donation to the metal surface. Topological analysis revealed weak hydrogen-bonding interactions within the molecules, potentially influencing their behavior. A negative Gibbs free energy (ΔG) indicates a spontaneous adsorption process, which is desirable for corrosion inhibitors. This study suggests that inhibitor molecules (E, M5, M6, M7) might transition from weak physical adsorption (physisorption) to stronger chemical adsorption (chemisorption) with increasing temperature. This chemisorption, characterized by stronger bonds between the inhibitor and metal surface, is crucial for effective corrosion inhibition. Estimated absorption spectra suggest a correlation between high absorption (Uro M5) and potential susceptibility to corrosion, while lower absorption (Uro M7) might indicate better resistance. Finally, Fukui function analysis suggests that oxygen atoms with higher values could exhibit stronger adsorption capabilities. Overall, this study provides insights into the potential of urolithin derivatives as corrosion inhibitors and highlights the importance of considering various molecular properties for optimizing their effectiveness.

V. Acknowledgment

The author like to express our gratitude to Koya University's Chemistry Department for their assistance and support in our endeavor.

References

Abbaz, T., Bendjeddou, A., and Villemin, D., 2018. Molecular structure, NBO analysis, first-hyperpolarizability, and homo-lumo studies of π-extended tetrathiafulvalene (EXTTF) derivatives connected to π-nitro phenyl by density functional method. *International Journal of Advanced Chemistry*, 6, p.114-120.

Akman, F., Demirpolat, A., Kazachenko, A.S., Kazachenko, A.S., Issaoui, N., and Al-Dossary, O.J.M., 2023. Molecular Structure, Electronic Properties, Reactivity (ELF, LOL, and Fukui), and NCI-RDG Studies of the Binary Mixture of Water and Essential Oil of *Phlomis bruguieri*. *Molecules*, 28, p.2684

Arulaabaranam, K., Muthu, S., Mani, G., and Geoffrey, A.B., 2021. Speculative assessment, molecular composition, PDOS, topology exploration (ELF, LOL, RDG), ligand-protein interactions, on 5-bromo-3-nitropyridine-2-carbonitrile. *Heliyon,* 7, p.e07061.

Asath, R.M., Rekha, T., Premkumar, S., Mathavan, T., and Benial, A.M.F., 2016. Vibrational, spectroscopic, molecular docking and density functional theory studies on N-(5-aminopyridin-2-yl) acetamide. *Journal of Molecular Structure*, 1125, pp.633-642.

Asif, M., Sajid, H., Ayub, K., Gilani, M.A., Anwar, N., and Mahmood, T., 2023. Therapeutic potential of oxo-triarylmethyl (oxTAM) as a targeted drug delivery system for nitrosourea and fluorouracil anticancer drugs; A first principles insight.

Journal of Molecular Graphics and Modelling, 122, p.108469.

Bader, R.F., 2010. Definition of molecular structure: By choice or by appeal to observation? *The Journal of Physical Chemistry A*, 114, pp.7431-7444.

Becke, A.D., 1996. *Density-Functional Thermochemistry*. *Book of Abstracts, 212th ACS National Meeting*, Orlando, FL.

Boughoues, Y., Benamira, M., Messaadia, L., and Ribouh, N., 2020. Adsorption and corrosion inhibition performance of some environmental friendly organic inhibitors for mild steel in HCl solution via experimental and theoretical study. *Colloids and Surfaces A: Physicochemical and Engineering Aspects*, 593, p.124610.

Boukabcha, N., Benmohammed, A., Belhachemi, M.H.M., Goudjil, M., Yahiaoui, S., Megrouss, Y., Djafri, A., Khelloul, N., Benyehlou, Z.D., and Djafri, A., 2023. Spectral investigation, TD-DFT study, hirshfeld surface analysis, NCI-RDG, HOMO-LUMO, chemical reactivity and NLO properties of 1-(4-fluorobenzyl)-5-bromolindolin-2, 3dione. *Journal of Molecular Structure*, 1285, p.135492.

Caid, Z.A.E., Left, D.B., Thoume, A., Kellal, R., and Zertoubi, M., 2023. A comprehensive computational study of N-phenylacetamide derivatives as corrosion inhibitors for copper: Insights from DFT and Molecular Dynamics. *Journal of Bio-and Tribo-Corrosion*, 9, p.83.

Chen, C., Jiang, L., Guo, M.Z., Xu, P., Chen, L., and Zha, J., 2019. Effect of sulfate ions on corrosion of reinforced steel treated by DNA corrosion inhibitor in simulated concrete pore solution. *Construction and Building Materials*, 228, p.116752.

Dennington, R., Keith, T.A., and Millam, J.M., 2016. *GaussView, Version 6.0. 16*. Semichem Inc., Shawnee Mission KS.

Domingo, L.R., Aurell, M.J., Pérez, P., and Contreras, R., 2002. Quantitative characterization of the global electrophilicity power of common diene/dienophile pairs in Diels-Alder reactions. *Tetrahedron*, 58, pp.4417-4423.

Ech-Chihbi, E., El Hajjaji, F., Titi, A., Messali, M., Kaya, S., Serdaroğlu, G., Hammouti, B., and Taleb, M., 2024. Towards understanding the corrosion inhibition mechanism of green imidazolium-based ionic liquids for mild steel protection in acidic environments. *Indonesian Journal of Science and Technology*, 9, pp.395-420.

El Aoufir, Y., El Bakri, Y., Lgaz, H., Zarrouk, A., Salghi, R., Warad, I., Ramli, Y., Guenbour, A., Essassi, E., and Oudda, H., 2017. Understanding the adsorption of benzimidazole derivative as corrosion inhibitor for carbon steel in 1 M HCl: Experimental and theoretical studies. *Journal of Materials and Environmental Science*, 8, pp.3290-3302.

Fan, B., Zhao, X., Liu, Z., Xiang, Y., and Zheng, X., 2022. Inter-component synergetic corrosion inhibition mechanism of Passiflora edulia Sims shell extract for mild steel in pickling solution: Experimental, DFT and reactive dynamics investigations. *Sustainable Chemistry and Pharmacy*, 29, p.100821.

Fayomi, O.M., Chahul, H.F., Ike, D.C., Ndukwe, G.I., and Phoebe, I.M., 2021. Thermodynamic and adsorption study of the corrosion inhibition of mild steel by aframomum chrysanthum extract in 0.1 M hydrochloric acid solution. *Asian Journal of Applied Chemistry Research,* 8, pp.64-73.

Frisch, M., Clemente, F.M.J., Frisch, G.W., Trucks, H.B., Schlegel, G.E., Scuseria, M.A., Robb, J.R., Cheeseman, G., Scalmani, V., Barone, B., Mennucci, G.A., Petersson, H., Nakatsuji, M., Caricato, X., Li, H.P., Hratchian, A.F., Izmaylov, J., Bloino, G., Zheng, J.L., Sonnenberg, M., Hada, M., Ehara, K., Toyota, R., Fukuda, J., Hasegawa, M., Ishida, T., Nakajima, Y., Honda, O., Kitao, H., Nakai, T., Vreven, J.A., Montgomery, J.E. Jr., Peralta, F., Ogliaro, M., Bearpark, J.J., Heyd, E., Brothers, K.N., Kudin, V.N., Staroverov, T., Keith, R., Kobayashi, J., Normand, K., Raghavachari, A., Rendell, J.C., Burant, S.S., Iyengar, J., Tomasi, M., Cossi, N., Rega, J.M., Millam, M., Klene, J.E., Knox, J.B., Cross, V., Bakken, C., Adamo, J., Jaramillo, R., Gomperts, R.E., Stratmann, O., Yazyev, A.J., Austin, R., Cammi, C., Pomelli, J.W., Ochterski, R.L., Martin, K., Morokuma, V.G., Zakrzewski, G.A., Voth, P., Salvador, J.J., Dannenberg, S., Dapprich, A.D., Daniels, O., Farkas, J.B., Foresman, J.V., Ortiz, J., Cioslowski, D.J., 2013. *Fox*, *Gaussian 09*, *Revision D.01*. Gaussian Inc., Wallingford.

Frisch, M.J., Pople, J.A., and Binkley, J.S., 1984. Self-consistent molecular orbital methods 25. Supplementary functions for Gaussian basis sets. *The Journal of Chemical Physics*, 80, pp.3265-3269.

Gowers, R.J., Farmahini, A.H., Friedrich, D., and Sarkisov, L., 2018. Automated analysis and benchmarking of GCMC simulation programs in application to gas adsorption. *Molecular Simulation,* 44, pp.309-321.

Guruprasad, A., Sachin, H., Swetha, G., and Prasanna, B., 2020. Corrosion inhibition of zinc in 0.1 M hydrochloric acid medium with clotrimazole: Experimental, theoretical and quantum studies. *Surfaces and Interfaces*, 19, pp.100478

Hamad, A.R., Ahmed, K.M., Omer, R.A., Azeez, Y.H., Kareem, R.O., Othman, K.A., and Amin, A.A., 2025. Synthesis, characterization and computational study of thiourea-based dihydropyrimidine derivatives: A focus on adsorption and reactivity. *Journal of Molecular Structure*, 1325, p.140950.

Hameed, R.A., Abu-Nawwas, A.A.H., and Shehata, H., 2013. Nano-composite as corrosion inhibitors for steel alloys in different corrosive media. *Advances in Applied Science Research,* 4, pp.126-129.

Hazani, N.N., Mohd, Y., Ghazali, S.A.I.S.M., Farina, Y., and Dzulkifli, N.N., 2019. Electrochemical studies on corrosion inhibition behaviour of synthesised 2-acetylpyridine 4-ethyl-3-thiosemicarbazone and its Tin (IV) complex for mild steel in 1 M HCl solution. *Journal of Electrochemical Science and Technology*, 10, pp.29-36.

Hekim, S., Azeez, Y.H., and Akpinar, S., 2019. The theoretical investigation of the HOMO, LUMO energies and chemical reactivity of C9H12 and C7F3NH5Cl molecules. *Journal of Physical Chemistry and Functional Materials*, 2, pp.29-31.

Hssain, A., 2022. DFT modelling studies of spectroscopic properties and medium effects on molecular reactivity of secnidazole in different solvents. *Journal of Physical Chemistry and Functional Materials*, 5, pp.69-83.

Humphrey, W., Dalke, A., and Schulten, K., 1996. VMD: Visual molecular dynamics. *Journal of Molecular Graphics,* 14, pp.33-38, 27-28.

İsen, F., Kaygili, O., Bulut, N., Ates, T., Osmanlıoğlu, F., Keser, S., Tatar, B., Özcan, I., Ates, B., and Ercan, F., 2023. Experimental and theoretical characterization of Dy-doped hydroxyapatites. *Journal of The Australian Ceramic Society*, 59, pp.849-864.

Jumabaev, A., Holikulov, U., Hushvaktov, H., Issaoui, N., and Absanov, A., 2023. Intermolecular interactions in ethanol solution of OABA: Raman, FTIR, DFT, M062X, MEP, NBO, FMO, AIM, NCI, RDG analysis. *Journal of Molecular Liquids*, 377, p.121552.

Kareem, R.O., Omer, R.A., Ahmed, K.M., and Azeez, Y.H., 2024. DFT and Monte Carlo simulation studies of potential corrosion inhibition properties of some basic heterocyclic compounds. *Molecular Simulation,* 50, pp.1447-1464.

Koparir, P., Omar, R.A., Sarac, K., Ahmed, L.O., Karatepe, A., Taskin-Tok, T., and Safin, D.A., 2023. Synthesis, characterization and computational analysis of thiophene-2, 5-diylbis ((3-mesityl-3-methylcyclobutyl) methanone. *Polycyclic Aromatic Compounds*, 43, pp.6107-6125.

Korkmaz, A.A., Ahmed, L.O., Kareem, R.O., Kebiroglu, H., Ates, T., Bulut, N., Kaygili, O., and Ates, B., 2022. Theoretical and experimental characterization of Sn-based hydroxyapatites doped with Bi. *Journal of the Australian Ceramic Society*, 58, pp.803-815.

Krishnan, R., Binkley, J.S., Seeger, R., and Pople, J.A., 1980. Self-consistent molecular orbital methods. XX. A basis set for correlated wave functions. *The Journal of Chemical Physics*, 72, pp.650-654.

Lu, T., and Chen, F., 2012. Multiwfn: A multifunctional wavefunction analyzer. *Journal of Computational Chemistry*, 33, pp.580-592.

Mamad, D.M., Omer, R.A., and Othman, K.A., 2023a. Quantum chemical analysis of amino acids as anti-corrosion agents. *Corrosion Reviews*, 41, pp.703-717.

Mamad, D.M., Rasul, H.H., Awla, A.H., and Omer, R.A., 2023b. Insight into corrosion inhibition efficiency of imidazole-based molecules: A quantum chemical study. *Doklady Physical Chemistry*, 511, pp.125-133.

Mamand, D.M., Azeez, Y.H., and Qadr, H.M., 2023. Monte carlo and DFT

calculations on the corrosion inhibition efficiency of some benzimide molecules. *Mongolian Journal of Chemistry*, 24, pp.1-10.

Merdas, S.M., 2021. Synthesis, characterization and DFT studies of new Azo-Schiff base and evaluation as corrosion inhibitor. *Annals of the Romanian Society for Cell Biology*, 25, pp.910-928.

Metropolis, N., Rosenbluth, A.W., Rosenbluth, M.N., Teller, A.H., and Teller, E., 1953. Equation of state calculations by fast computing machines. *The Journal of Chemical Physics*, 21, pp.1087-1092.

Murthy, Z.V.P., and Vijayaragavan, K., 2014. Mild steel corrosion inhibition by acid extract of leaves of *Hibiscus sabdariffa* as a green corrosion inhibitor and sorption behavior. *Green Chemistry Letters and Reviews*, 7, pp.209-219.

Mustafa, M.D., and Mohammad, Q.H., 2023. Quantum chemical and monte carlo simulations on corrosion inhibition efficiency of 2-mercapto-5-phenylfuran and bis (pyridyl) oxadiazoles. *Izvestiya Vysshikh Uchebnykh Zavedeniy Khimiya Khimicheskaya Tekhnologiya*, 66, pp.33-45.

Nam, K., Gao, J., and York, D.M., 2005. An efficient linear-scaling Ewald method for long-range electrostatic interactions in combined QM/MM calculations. *Journal of Chemical Theory and Computation*, 1, pp.2-13.

Norouzbahari, M., Burgaz, E.V., Ercetin, T., Fallah, A., Foroumadi, A., Firoozpour, L., Sahin, M.F., Gazi, M., and Gulcan, H.O., 2018. Design, synthesis and characterization of novel urolithin derivatives as cholinesterase inhibitor agents. *Letters in Drug Design and Discovery*, 15, pp.1131-1140.

Omer, R.A., Ahmed, K.M., Othman, K.A., Hamad, W.M., Faraj, R.K., Muhialdin, A.J., and Salih, S.K., 2024. New thiazole derivatives. *Aro-The Scientific Journal of Koya University*, 12, pp.10-22.

Özbakır Işin, D., Karakuş, N., Lgaz, H., Kaya, S., and Chung, I., 2020. Theoretical insights about inhibition efficiencies of some 8-Hydroxyqionoline derivatives against the corrosion of mild steel. *Molecular Simulation,* 46, pp.1398-1404.

Predko, P., Rajnovic, D., Grilli, M.L., Postolnyi, B.O., Zemcenkovs, V., Rijkuris, G., Pole, E., and Lisnanskis, M., 2021. Promising methods for corrosion protection of magnesium alloys in the case of Mg-Al, Mg-Mn-Ce and Mg-Zn-Zr: A recent progress review. *Metals*, 11, p.1133.

Qader, İ.N., Mohammad, A., Azeez, Y.H., Agid, R.S., Hassan, H.S., and Al-Nabawi, S.H.M., (2019). Chemical structural and vibrational analysis of potassium acetate: A density function theory study. *Journal of Physical Chemistry and Functional Materials*, 2, pp.23-25.

Qadr, H.M., and Mamand, D.M., 2023. A computational study of substituent effect 1, 3, 4-thiadiazole on corrosion inhibition. *Azerbaijan Chemical Journal*, pp.19-29.

Rani, B., and Basu, B.B.J., 2012. Green inhibitors for corrosion protection of metals and alloys: An overview. *International Journal of Corrosion*, 2012, p.380217.

Rasul, H.H., Mamad, D.M., Azeez, Y.H., Omer, R.A., and Omer, K.A., 2023. Theoretical investigation on corrosion inhibition efficiency of some amino acid compounds. *Computational and Theoretical Chemistry*, 1225, p.114177.

Razali, N.Z.K., Wan Hassan, W.N.S., Sheikh Mohd Ghazali, S.A.I., Mohd Shotor, S.N., and Dzulkifli, N.N., 2023. DFT, Fukui indices, and molecular dynamic simulation studies on corrosion inhibition characteristics: A review. *Chemical Papers*, 78, pp.1-17.

Rozas, I., Alkorta, I., and Elguero, J., 2000. Behavior of ylides containing N, O, and C atoms as hydrogen bond acceptors. *Journal of the American Chemical Society*, 122, pp.11154-11161.

Saidj, M., Djafri, A., Rahmani, R., Belkafouf, N.E.H., Boukabcha, N., Djafri, A., and Chouaih, A., 2023. Molecular structure, experimental and theoretical vibrational spectroscopy,(HOMO-LUMO, NBO) investigation,(RDG, AIM) analysis,(MEP, NLO) study and molecular docking of Ethyl-2-{[4-Ethyl-5-(Quinolin-8-yloxyMethyl)-4H-1, 2, 4-Triazol-3-yl] sulfanyl} acetate. *Polycyclic Aromatic Compounds*, 43, pp.2152-2176.

Salih, S.K., Mustafa, R.M., Mamad, D.M., Kaka, K.N., Omer, R.A., and Hamad, W.M., 2023. Synthesis of liquid crystalline benzothiazole based derivatives: Theoretical and experimental study of their optical and electrical properties. *ZANCO Journal of Pure and Applied Sciences*, 35, pp.143-162.

Srivastavaa, A., Kumara, V., Vermaa, A., Guptaa, M., and Dubeya, Y., 2019. Kinetic, Mechanistic and quantum chemical calculations of Ru (III) catalysed redox reaction of aspirin by nbs in acidic medium. *Journal of Information and Computational Science*, 9, pp.516-540.

Sujatha, H., and Lavanya, M., 2023. An insight to HOMO LUMO aspects in corrosion applications. *Canadian Metallurgical Quarterly*, 62, pp.761-772.

Sun, H., 1998. COMPASS: An ab initio force-field optimized for condensed-phase applications overview with details on alkane and benzene compounds. *The Journal of Physical Chemistry B*, 102, pp.7338-7364.

Sun, H., Jin, Z., Yang, C., Akkermans, R.L., Robertson, S.H., Spenley, N.A., Miller, S., and Todd, S.M., 2016. COMPASS II: Extended coverage for polymer and drug-like molecule databases. *Journal of Molecular Modeling*, 22, pp.1-10.

Sun, H., Ren, P., and Fried, J., 1998. The compass force field: Parameterization and validation for phosphazenes. *Computational and Theoretical Polymer Science*, 8, pp.229-246.

Tang, L., and Zhu, W., 2021. Computational design of high energy RDX-based derivatives: Property prediction, intermolecular interactions, and decomposition mechanisms. *Molecules*, 26, p.7199.

Tasić, Ž.Z., Petrović Mihajlović, M.B., Radovanović, M.B., and Antonijević, M.M., 2019. New trends in corrosion protection of copper. *Chemical Papers*, 73, pp.2103-2132.

Uwiringiyimana, E., Joseph, I.V., and ADams, F.V., 2016. The effect of corrosion inhibitors on stainless steels and aluminium alloys: A review. *African Journal of Pure and Applied Chemistry*, 10, pp.23-32.

Xiangrong, X., Zhuanhong, L., and Lei, Y., 2023. The synthesis of urolithins and their derivatives and the modes of antitumor action. *Mini-Reviews in Medicinal Chemistry,* 23, pp.80-87.

Yıldız, C.A., Güney, E., Nasif, V., Karakaş, D., and Erkan, S., 2023. Investigation of substituent effect on rhenium complexes by DFT methods: Structural analysis, IR spectrum, quantum chemical parameter, NLO and OLED properties, molecular docking. *Journal of Molecular Structure*, 1278, p.134835.

Yousif, H.A, and Hanaa, S.H., 2021b. Theoretical study for chemical reactivity descriptors of tetrathiafulvalene in gas phase and gas phase and solvent phases based on density functional theory. *Passer Journal of Basic and Applied Sciences*, 3, pp.167-173.

Yousif, H.A., and Hanaa, S.H., 2021a. Theoretical study for chemical reactivity descriptors of tetrathiafulvalene in gas phase and gas phase and solvent phases based on density functional theory. *Passer Journal of Basic and Applied Sciences*, 3, pp.167-173.